Parametric Mesh Study: Lucy Ashton Case

Matija Vasilev
Research Assistant
University of Belgrade
Faculty of Mechanical Engineering

Milan Kalajdžić
Full Professor
University of Belgrade
Faculty of Mechanical Engineering

This study considers the ship Lucy Ashton, a benchmark case providing full-scale measurements of total ship resistance and boundary layer thickness. A series of CFD simulations was carried out for several different scales and Froude numbers, with the aim of reproducing experimental data on ship resistance and the boundary layer. The results showedagreement with the measurements, with ship resistance predictions within ±5% and realistic boundary layer profiles along the hull. Based on these findings, practical formulas for boundary layer thickness and base mesh cell size were derived. Although these formulas were developed considering only the Lucy Ashton case, they represent a promising basis for application to other ships, particularly at model scale. Further studies are recommended to confirm their reliability for different fullscale hull forms.

Keywords: *mesh, boundary layer, full-scale, model scale, resistance prediction.*

1. INTRODUCTION

1.1 CFD mesh

Computational Fluid Dynamics (CFD) has become very useful tool in the last decade for improving ship hydrodynamics and reducing operational costs in the shipping industry. CFD enables detailed analysis of ship hull and propeller performance, directly addressing economic and regulatory pressures to minimize fuel consumption and therefore, improve energy efficiency. In addition to the CFD (numerical) approach commonly used for the analysis of ship energy efficiency, analytical methods are also available [1], [2].

Parametric mesh studies in ship CFD are essential for ensuring accuracy while optimizing computational efficiency. Research shows that mesh generation and resolution directly impact simulation results. When studying ship resistance, researchers have successfully used multiple mesh configurations ranging from coarse to fine grids, comparing results to validate the compu–tational approach [3]. Similarly, analysis of mesh reso–lution effects demonstrates that mesh configuration directly impacts numerical results in velocity fields, with finer meshes showing convergence improvements of up to 6.4% [4]. One comprehensive study conducted over 50 iterations of heaving sphere simulations by varying mesh configurations and simulation parameters, achieving good agreement with experimental data while maintaining computational efficiency through axisym–metric exploitation [5]. In resistance prediction studies, parametric analysis has revealed that wavelength ratio significantly influences the pattern of resistance in waves, with added resistance behaviour varying non-linearly with wave height [6]. Grid-independence stu–dies are essential to establish which mesh configurations provide adequate accuracy, and modern approaches increasingly employ machine learning to guide parametric optimization searches efficiently [7]. Grid sensitivity (or grid convergence) studies evaluate how variations in mesh resolution affect simulation results. The standard approach uses Richardson extrapolation methods to assess mesh convergence. In ship hydro–dynamics, researchers typically conduct systematic grid convergence studies based on multiple grid resolutions to predict uncertainties in numerical solutions [8]. A key protocol involves performing sensitivity analyses on each operating condition, with particular attention paid to critical flow regions like the free-surface and wake fields in the propeller plane. When conducting grid refinement studies, researchers evaluate sensitivity for each operating condition separately. For example, in full-scale ship trials, grid refinement sensitivity is systematically assessed for each power setting, and time-step effects are also evaluated for the selected grids. The simulated results showed good agreement with test data, illustrating the capability of numerical methods to determine ship performance at full scale[9]. Studies investigating ship resistance and self-propulsion often verify grid convergence through comparison with experimental data, examining the influence of factors like mesh density, time steps, and turbulence models [10]. The free-surface region and wake flow require particular mesh refinement. Grid independence studies should assess both overall domain resolution and local refinement at critical areas [11]. Additionally, research on ship design operations in confined waters has utilized detailed grid independence checks at different design stages to optimize both accuracy and computational efficiency [12].

A comprehensive study by [13]. developed best practices for self-propulsion simulation of ship models in calm water. Extensive convergence studies were carried out to examine effects of various propeller mod–

Received: February 2026, Accepted: March 2026
Correspondence to: Matija Vasilev, University of Belgrade, Faculty of Mechanical Engineering, Kraljice Marije 16, 11120 Belgrade, Serbia
E-mail: mnvasilev@mas.bg.ac.rs
doi: 10.5937/fme2602245V

elling methods and parameters, including non-dimen–sional wall distance, grid resolution/distribution, and turbulence model selection. The study examined both bare-hull resistance and propeller open-water perfor–mance initially, then applied two different propeller modelling methods: a simplified body-force method and a detailed propeller modelling approachto predict wake fraction and propeller performance behind the hull. The difference in accuracy between these methods was quantified through convergence studies, allowing rese–archers to establish best modelling practices. Validation was performed on the KRISO Container Ship (KCS) model, where the effective wake fraction determined from CFD was compared with experimental effective wake fraction data. A detailed numerical study on full-scale ship self-propulsion performance demonstrates how grid convergence is incorporated into validation procedures [14]. The research included simulations using RANS method with both double-model and Volume-of-Fluid (VOF) models for scale effect analysis. Verification of grid convergence was perfor–med through global mesh refinements, and a series of sea trials were conducted to collect reliable data for validating predictions. The study demonstrated that grid convergence studies are critical for understanding hull-propeller interaction, where boundary layer separation is the main source of wake variation. Notably, the research found that simplification of free surface treatment does not only affect wave-making resistance of the bare hull but also induced drag, which can produce up to 5% uncertainty in power prediction. A numerical study of two-propeller hydrodynamic performance demonstrates systematic grid convergence methodology [15]. The research conducted standardized mesh and time-step convergence studies following ITTC recommendations. The hydrodynamic results for the KP505 propeller were compared with experimental data to validate the reliability of the method. Over 40 propeller arrangements with varying transverse and longitudinal spacing were then simulated. The study revealed that the high-speed wake generated by the upstream propeller significantly affects the downstream propeller's hydrodynamic performance, with this interaction diminishing as transverse spacing increases. An uncertainty quantification study of self-propulsion analyses with RANS-CFD examined a small-size product/oil tanker at model scale [16]. The methodology involved open water propeller predictions and model scale computations for minimum two different loadings to determine the self-propulsion point and respective parameters. To expedite computations, cases were solved using a single-phase approach. Resistance predictions were compared with experimental findings, and uncertainty associated with thrust prediction was quantified. The comparison between CFD predictions and full-scale sea trials conducted on the subject ship indicated that CFD computation could predict performance with sufficient accuracy at acceptable computational cost. A study on Flettner rotors as wind-assisted propulsion demonstrated grid convergence methodology for preliminary design assessment [17]. RANS-based CFD evaluated aerodynamic performance of various rotor configurations. A grid convergence study was conducted as part of the CFD results verifi–cation process. Initially, isolated 2D and 3D rotors at model scale were simulated for various operating conditions. A cargo ship fitted with Flettner rotors was then simulated to compute resistance and evaluate rotor-to-rotor interaction, demonstrating how grid conver–gence studies enable confidence in subsequent design evaluations.

These examples demonstrate that grid sensitivity studies are essential at every stage of ship CFD analysis, from preliminary design through validation against sea trials. The studies consistently show that proper mesh convergence procedures establish confidence in propul–sion performance predictions, enable accurate scale effects analysis, and support design optimization with quantified uncertainty bounds.

1.2 Boundary layer

The boundary layer forms on the ship's hull surface because of the fluid's viscous effects, causing the fluid velocity to change from zero at the solid surface to the value of the undisturbed flow velocity. The exact characteristics of the boundary layer depend on factors such as the Reynolds number, ship geometry, speed and fluid properties. Its study is crucial for determining the frictional resistance coefficient, which represents a significant component of the ship's total resistance. It is known that when the hull is subjected to water flow, turbulent flow occurs and consequently, the boundary layer that forms is called the turbulent boundary layer. The boundary layer thickness is defined as the position where the flow velocity reaches 99% of the undisturbed flow velocity, measured from the wall where the flow velocity is zero [18].

Research in the field of boundary layer velocities dates back more than 120 years [19-21] and initially focused on pipe flow. It was concluded that the velocity near the wall during turbulent flow varies with 1/7 power of the distance from the wall. It should be noted that this exponent holds only for smooth pipes (up to Re = 10□), but for larger Reynolds numbers, it decreases to 1/10. However, in the case of rough pipes, the exponent for increasing relative roughness rises from 1/7 to 1/4 [22]. As early as 1927, Prandtl proposed an expression for the thickness of the turbulent boundary layer in pipes [20]:

$$\frac{\delta}{x} \approx \frac{0.37}{\mathrm{Re}_x^{1/5}} \tag{1}$$

For flow over a flat plate, the following expressions were obtained [23]:

$$\frac{\delta}{x} \approx \frac{0.16}{\mathrm{Re}_x^{1/7}} \tag{2}$$

or [24]:

$$\frac{\delta}{x} = \frac{0.382}{\mathrm{Re}_x^{1/5}} \tag{3}$$

Since a ship has an extraordinarily complex geo–metric structure, the turbulent boundary layer that forms

is highly irregular in shape [25]. In 1948, one of the first formulations for the boundary layer thickness on ships appeared [26,27]:

$$\delta = \frac{5.5x}{\sqrt{\mathrm{Re}}} \tag{4}$$

By the 1970s, research emerged focusing on methods for solving three-dimensional turbulent boundary layer flow on ships [28] which later led to the organization of the first workshop in 1980 [29]. The greatest challenge when solving flow around a ship's hull arises in the stern region where flow separation occurs [30]. In [31] authors conducted experiments in a wind tunnel on a 10ft long Wigley hull to study the flow in the boundary layer and a wake over the stern. Study by [32] presents experimental results from towing-tank tests examining propeller-hull interaction using the Series 60 C_b = 0.6 hull form. Measurements included mean-velocity and pressure fields for conditions both with and without a propeller. Data were collected upstream, downstream and in the near-wake region, alongside surface-pressure distributions, wave profiles, resistance and self-propulsion tests. Results highlight key differences in flow behaviour when a propeller is present. The interaction between the propeller and the hull's boundary layer and wake is analysed using a propeller-performance program, revealing that most interaction effects stem from the propeller's response to the three-dimensional non-uniform inflow.

Boundary layer phenomena are critical in maritime applications as they affect resistance, propulsion set and manoeuvrability. Accurate simulation of these phenomena requires sufficiently refined and well-structured meshes that capture the near-wall effects effectively. The advances in mesh generation techniques have notable implications for maritime CFD analyses. In [33] authors discussed how the future landscape of CFD will rely on high-performance computing and improved mesh adaptability, proposing that real-time simulations will depend on the efficiency and quality of generated meshes. This interdependence inherently calls for innovative solutions to align meshing techniques with complex geometries and fluid interactions in maritime settings.

One critical challenge in ship hydrodynamics is managing the significant difference in boundary layer thickness between model-scale and full-scale ships. A novel approach to address this is the Boundary Layer Similarity (BLS) model, where only the stern part of the hull is extracted and lengthened to make its boundary layer thickness equivalent to that of a full-scale ship [34]. CFD simulations of energy-saving fin performance demonstrated that the BLS model is capable of predicting full-scale performance through model-scale simulations, with flow fields affected by fins showing similar characteristics to those of full-scale ships

Different turbulence models have varying capabilities for capturing boundary layer characteristics. Research comparing eight turbulent viscous models revealed that model selection significantly affects the prediction of pressure distribution, velocity distribution, and boundary layer characteristics around ship hulls [35].

The boundary layer separation around the hull is a primary source of wake variation and affects propeller performance. Research on full-scale ship self-propulsion demonstrated that the difference in hull boundary layer separation is the main source of wake characteristics [14]. This finding links boundary layer behaviour directly to propulsive efficiency. In shallow water operations, the boundary layer interactions become even more complex; studies found that the ship's manoeuvring characteristics in shallow water are linked to complex interactions between the hull wake, boundary layer, propeller, vortices, and the seabed [36].

Currently, the literature does not provide specific guidance on the mesh resolution of the near-wall region for ship applications. The need for such guidance arises from the fact that CFD software often requires this value as an input when generating the mesh. Three key parameters are commonly used as inputs when defining the mesh in the near-wall region: the prism layer total thickness, the number of layers and either the aspect ratio or the thickness of the first layer. The number of layers determines how many individual mesh layers are included within near-wall region. A higher number of layers can improve the resolution of the velocity profile but may increase computational costs. Conversely, too few layers may result in insufficient resolution, compromising simulation accuracy.

Some studies provide guidance on the appropriate size of the base cell. The base cell size plays a significant role in defining the overall mesh structure and balancing computational efficiency with solution accuracy. In the study that involves estimating the resistance of a catamaran using CFD software [37] it is suggested that a grid size of about 6.0‰ of the waterline length can be used as the mesh size for the catamaran surface. The study [38] identifies that a grid size of 0.34% of the waterline length optimizes resistance prediction accuracy without increasing computational cost and resistance results remain stable with y^+ values between 11.5 and 200. Additionally, while the grid distribution ratio has minimal impact under these conditions, a smaller ratio is recommended for improved accuracy.

This study focuses on the Lucy Ashton benchmark, selected due to the availability of extensive experimental data, including resistance measurements at multiple model scales, full-scale resistance data, and boundary layer thickness measurements. Results from the Workshop are summarized in [39], while other research based on this ship are presented in [40], [41].Lucy Ashton, a former paddle steamer built in 1888, was extensively modified after 1949 for full-scale resistance experiments, including hull fairing and the installation of four jet engines to provide steady, well-controlled thrust. The experimental database originates from 1950s sea trials conducted at multiple speeds and under different surface conditions; for the workshop, the smoothest configuration (faired seams with aluminium paint) was adopted as the reference case, without roughness modelling in CFD. Ship speed and boundary-layer characteristics were measured using pitot logs mounted at two longitudinal positions along the hull. The measured velocity profiles confirmed the expected

growth of the boundary layer downstream and yielded frictional resistance estimates consistent with direct resistance measurements.

Based on the results of conducted Lucy Ashton case, the objectives of this study are defined as follows:

- To analyze the boundary layer thickness of the Lucy Ashton case through CFD results and compare its variation with Reynolds number against classical theoretical formulations (1-4);
- To determine an appropriate distribution of layers in the near-wall region for accurate CFD resolution of flow close to the surface;
- Formulation of an expression for the base cell size in the mesh;
- Validation of the developed methods using experi–mental data from the Lucy Ashton ship in various model scales and full scale.

2. METHODOLOGY

2.1 Case description

The Lucy Ashton case is particularly well suited for addressing the points outlined above due to the availability of experimental data. This includes total resistance measurements from model tests at six different scales and across multiple speeds λ = [21.167, 15.875, 11.906, 9.525, 7.938, 6.35], total resistance data for several speeds in full scale (λ = 1), and boundary layer thickness measurements at a speed of 10.18 knots, taken at 49% of the ship length from the stern along the centerline. The basic data and dimensions of the Lucy Ashton ship are provided in the following Table 1.

Table 1. Ship particulars

L_{pp} [m]	58.1
L_{wl} [m]	59.49
B [m]	6.4
T [m]	1.584
H [m]	2.1844
WS_{total} [m^2]	417
Δ [t] (sw)	390
C_b [-]	0.685
C_p [-]	0.705
C_m [-]	0.972

2.2 CFD setup and simulation conditions

The initial speeds considered for the CFD analysis in this study are the same as those used in the workshop, with Fr = [0.130, 0.173, 0.219, 0.260, 0.304] for the full-scale ship and Fr = 0.219 for the model scale. For the CFD calculations, the software STAR-CCM+ developed by Siemens was used. In wall-resolved mesh generation, three key parameters are commonly defined to control the near-wall discretization: the number of prism (inflation) layers, the near-wall (first-layer) thickness and the total prism layer thickness. There is a mathematical relationship between these three para–meters, which is based on geometric progression:

$$\delta_{\text{pltt}} = \frac{Y_1\left(1-\text{SF}^{n_{\text{lay}}}\right)}{1-SF} \tag{5}$$

where δ_{pltt} is the prism layer total thickness, Y_1 is the thickness of the first cell layer, SF is the stretch factor and n_{lay} is the number of layers, representing four unknown quantities. Since there are no recommen–dations for the prism layer total thickness of complex geometric shapes, recommendations for boundary layer thickness in pipes or flat plates (1-4) are usually used, where x is the length of the ship at the waterline (L_{wl}) and Re is the Reynolds number based on the length at the waterline. This region is defined prior to running the simulation and does not need to match the actual boundary layer thickness for a specific ship. This is the reason why the same symbol is used for the total prism layer thickness (δ_{pltt}) and boundary layer thickness (δ). There are no direct recommendations for determining the thickness of the first cell layer, but there is a relationship between this parameter and the dimensionless thickness of the first cell layer, y^+.

$$y^+ = \frac{Y_1 u^*}{v} \tag{6}$$

where u^* is the friction velocity and v is the kinematic viscosity of water. The kinematic viscosity can be determined based on the temperature of the water at which the experiments were conducted. In this case, it was determined based on known values for density and dynamic viscosity (given in Table 2).

Table 2. Water and air properties

	Full scale	Model scale
ρ_w [kg/m^3]	1026.02	998.8
ρ_a [kg/m^3]	1.225	1.242
η_w [Pas]	1.22E-03	1.27E-03
η_a [Pas]	1.79E-05	1.77E-05

The friction velocity can be determined using the following expression:

$$u^* = \sqrt{\frac{\tau_w}{\rho_w}} \tag{7}$$

where τ_w is the wall shear stress (viscous force stress on the wall or ship hull), which can be determined using the following expression:

$$\tau_w = \frac{1}{2} C_V \rho_w u^2 \tag{8}$$

where C_V is the coefficient of viscous resistance and u is the free-stream velocity of water (i.e., the speed of the ship). The coefficient of viscous resistance, according to the ITTC 1978, is determined by the following formula [42]:

$$C_V = (1+k) C_F \tag{9}$$

where k is the form factor and C_F is the friction coefficient for an equivalent flat plate, which can be determined using the ITTC formula [42]:

$$C_F = \frac{0.075}{(\log \text{Re} - 2)^2} \tag{10}$$

Form factor is extracted with Prohaska's method as indicated in the [43]. If data for the form factor is not available, empirical formulas given in [44] can be used, or recommendations provided in [45]. Also, CFD double body simulations can be used to determine the form factor [46].

2.3 Mesh parameterization

Based on the current guidelines and recommendations [47], which emphasize that y^+ should remain within the range of 30 to 100 for CFD simulations in ship hydrodynamics if wall functions are used, the question arises of how to determine the parameters used as input for setting up such simulations. This study demonstrates one possible approach to defining these parameters. In addition to y^+, there is a specified *SF* in [47] to be 1.2 and number of layers (n_{lay}) to be 15, but in this research, an investigation is extended to cover a range of *SF* from 1.2 to 1.4 and the range for n_{lay} from 7 to 25. An additional reason for extending the ranges lies in the author's experience: simulations aimed at predicting the resistance of complex ship forms for certain ship types either failed or required excessive computational time due to poor mesh quality, which resulted directly from using a fixed number of layers in the near-wall region. Removing prism layers near the hull, according to the author's observations, led to unreliable results that did not match experimental measurements. Moreover, key parameters, such as y^+, would fall outside the limits defined by official ITTC and IACS guidelines.

By extending (6) and multiplying by L_{wl}/Fr:

$$\frac{y^+ L_{wl}}{Y_1 Fr} = \frac{u^* L_{wl}}{v\lambda} = f(\lambda) \tag{11}$$

A graphical representation of the dependency $\frac{y^+ L_{wl}}{Y_1 Fr}$ for ships of different scales can be obtained. Similarly, the dependence $\frac{y^+ L_{wl}}{Y_1 Fr}(Fr)$ for ships of the same scale but at different speeds can also be plotted:

$$\frac{y^+ L_{wl}}{Y_1 Fr} = \frac{u^* L_{wl}}{v\lambda} = g(Fr) \tag{12}$$

The functions $f(\lambda)$ and $g(Fr)$ can be represented in the form $a\cdot\lambda^b$ and $c\cdot Fr^d$, respectively, where the coefficients *a*, *b*, *c* and *d* are determined by using logarithmic transformation and linear regression with the least squares method:

$$a = \exp\left(\frac{\sum_j\left(\ln\frac{y^+ L_{wl}}{Y_1}(j) - b\cdot\sum_j\left(\ln\lambda(j)\right)\right)}{l}\right) \tag{13}$$

$$b = \frac{l\sum_j\left(\ln\lambda(j)\cdot\ln\frac{y^+ L_{wi}}{Y_1}(j) - \sum_j\left(\ln\lambda(j)\right)\cdot\sum_j\left(\ln\frac{y^+ L_{wi}}{Y_1}(j)\right)\right)}{l\sum_j\left(\ln\lambda(j)\right)^2 - \left(\sum_j\ln\left(\lambda(j)\right)\right)^2} \tag{14}$$

$$c = \exp\left(\frac{\sum_j\left(y^+ L_{wl(j)}\right) - d\cdot\sum_j\left(\ln Fr(j)\right)}{l}\right) \tag{15}$$

$$d = \frac{l\sum_j\left(\ln Fr(j)\cdot\ln\frac{y^+ L_{wl}}{Y_1}(j)\right) - l\sum_j\left(\ln\left(Fr(j)\right)\cdot\sum_j\left(\ln\frac{y^+ L_{wl}}{Y_1}(j)\right)\right)}{l\sum_j\left(\ln Fr(j)\right)^2 - \left(\sum_j\ln\left(Fr(j)\right)\right)^2} \tag{16}$$

where *l* is the number of speeds (*Fr*) i.e., number of scale factors in specific case. For Lucy Ashton case, *l*=7 for *Fr*=idem=0.219 and *l*=5 for λ=idem=1. Counter *j* goes from 1 to *l*.

Based on the prism layer total thickness, stretch factor, the number of layers and using the geometric sum formula for finite number of array elements, the first layer thickness can be evaluated.

$$Y_1 = \frac{\delta_{\text{pllt}}(1-SF)}{1-SF^{n_{\text{lay}}}} \tag{17}$$

From (11) and (12), y^+ can be expressed as:

$$y^+ = \frac{Y_1\cdot Fr}{L_{wl}} f(\lambda) = \frac{Y_1\cdot Fr}{L_{wl}}\cdot a\cdot\lambda^b \tag{18}$$

$$y^+ = \frac{Y_1\cdot\lambda}{L_{wl}} g(Fr) = \frac{Y_1\cdot\lambda}{L_{wl}}\cdot c\cdot Fr^d \tag{19}$$

The thickness of the last layer (Y_{last}) can be expressed as:

$$Y_{\text{last}} = Y_1\cdot SF^{n_{\text{lay}}} \tag{20}$$

When the size of the base cell (*BS*) is taken to be equal to the size of the last cell in the prism layer divided by zone refinement factor (*ZR*), the following relationship applies:

$$BS = Y_{\text{last}} / ZR \tag{21}$$

Zone refinement is a factor that depends on the degree of fineness of the local mesh. Zonal refinement is essential for achieving accurate predictions of hydrodynamic forces by concentrating mesh resolution in regions near the hull and in wave-making zones, where flow gradients are highest. This approach optimizes computational efficiency, enabling detailed analysis of complex geometries and advanced turbulence models without prohibitive resource costs.

Figure 1 illustrates the refinement zones, parametrically defined as functions of the principal dimensions (L_{pp}, *B*, *T*). The volumetric dimensions of these refinement zones are provided in Table 3 together with domain size (refer to the end of the paper). All dimensions in Table 3 are specified with respect to the global coordinate system, located at the aft perpendicular and the keel centerline. Positive values are oriented in the positive *x*-axis direction, i.e., toward the bow. In this manner (Table 3), the zones are defined for half of the ship, which can be applied in cases where the ship is symmetric, as in the present case. Table 4 presents the relative percentages of the base cell size along the *x*, *y*, and *z* directions, respectively.

Table 3. Domain and zone refinements dimensions

	Aft edge	Fore edge	Aft Side	Fore Side	Bottom extrusion	Top extrusion
Domain	$-3.5 \cdot L_{pp} / \lambda$	$2 \cdot L_{pp} / \lambda$	$2 \cdot L_{pp} / \lambda$	$2 \cdot L_{pp} / \lambda$	$-2 \cdot L_{pp} / \lambda$	$0.5 \cdot L_{pp} / \lambda$
Free surface refinement	$-3.5 \cdot L_{pp} / \lambda$	$2 \cdot L_{pp} / \lambda$	$2 \cdot L_{pp} / \lambda$	$2 \cdot L_{pp} / \lambda$	$0.9 \cdot T / \lambda$	$1.1 \cdot T / \lambda$
Stern refinement	$-0.15 \cdot L_{pp} / \lambda$	$0.2 \cdot L_{pp} / \lambda$	$0.6 \cdot B / \lambda$	$0.6 \cdot B / \lambda$	$-0.2 \cdot T / \lambda$	$1.3 \cdot T / \lambda$
Fore refinement	$0.9 \cdot L_{pp} / \lambda$	$1.05 \cdot L_{pp} / \lambda$	$0.6 \cdot B / \lambda$	$0.6 \cdot B / \lambda - 0.15 \cdot L_{pp} / \lambda \cdot \tan(20)$	$-0.2 \cdot T / \lambda$	$1.3 \cdot T / \lambda$
Fine cone refinement	$-1.5 \cdot L_{pp} / \lambda$	$1.5 \cdot L_{pp} / \lambda$	$3 \cdot L_{pp} / \lambda \cdot \tan(20)$	$0.8 \cdot B / \lambda$	$0.7 \cdot T / \lambda$	$1.3 \cdot T / \lambda$
Coarse cone refinement	$-2.25 \cdot L_{pp} / \lambda$	$1.8 \cdot L_{pp} / \lambda$	$7.5 \cdot L_{pp} / \lambda \cdot \tan(20)$	$2 \cdot B / \lambda$	$0.5 \cdot T / \lambda$	$1.5 \cdot T / \lambda$

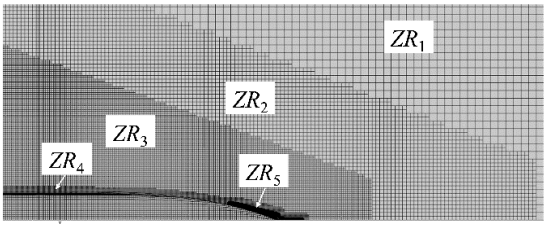

Figure 1. Zone refinements

Table 4. Zone refinements – Relative from base cell size

	ZR [% *BS*]		
	x	*y*	*z*
Domain	600	600	600
Free Surface	50	50	12.5
Stern refinement	12.5	12.5	12.5
Fore refinement	3.125	3.125	3.125
Fine cone refinement	12.5	12.5	6.25
Coarse cone refinement	25	25	12.5

In this specific case, it is applied that the degree of fineness of the last cell in the near-wall region is four, which means that the dimension of the last cell in the near-wall region is 6.25% of the base cell dimensions, i.e., it is 1/2□ times smaller.

The baseline equation for estimating the prism layer total thickness is given as (1), while assuming that the near-wall region thickness (i.e. prism layer total thickness) is equal to the boundary layer thickness and it was applied in first iteration. Alongside it, there are three other (17), (18) or (19) and (20) and five unknown variables (y^+, Y_1, SF, n_{lay}, Y_{last}), the system is not closed and cannot be solved analytically. However, since the ranges for y^+, SF andn_{lay} are defined, the system of equations can be solved by adding one additional condition. For a constant Fr and different scales, the one condition is that the product $Y_{\text{last}} \cdot \lambda$ should remain approximately constant across scales. This condition ensures that the physical size of the last layer in the near-wall region remains consistent in real dimensions across different scales, thereby maintaining similar wall resolution. In contrast, for constant scale and varying Fr, the last cells' sizes in the near-wall region i.e., the base cell size should remain approximately constant ($BS \approx const.$). In this way, one solution is selected for each scale or for each Fr. The resulting solution defines mesh parameters BS, y^+, Y_1 and n_{lay}, i.e., the full prism layer setup needed to generate an appropriate mesh.

The cell size in each case will be different (for different speeds or scales), so an additional analysis was performed to potentially develop a simple formula for determining its dimensions. The idea is to come up with a formula in the form $BS = f(L_{pp}, r, \lambda, m)$ where r is refinement level which according to [48] equals $\sqrt{2}$ (or 2, $2\sqrt{2}$,…) and m is the scaling parameter, which is sought such that it provides the largest cell dimension without significantly affecting the results. Specifically, m will be determined as a local minimum or maximum of the $h(\lambda)$ where h is approximated function for specific Fr:

$$h(\lambda) = BS \cdot \lambda / \left(L_{pp} \cdot r \right) \tag{22}$$

Thus, the suggested simple expression for the size of the base cell dimension will be in the form:

$$BS = (L_{pp} \cdot r / \lambda) \cdot m^s \tag{23}$$

where:

$$s = \begin{cases} 1, \text{if } h(\lambda) = 0 \text{ and } h(\lambda) < 0 \text{ (local maximum)} \\ -1, \text{if } h(\lambda) = 0 \text{ and } h(\lambda) > 0 \text{ (local minimum)} \\ 0, \text{otherwise} \end{cases}$$

and m is the local minimum or maximum of the function h.

2.4 Validation and boundary layer evaluation

As an output from the CFD analysis, two parameters are selected: the total resistance of the ship ($R_{T,\text{CFD}}$) and the dimensionless boundary layer thickness $\delta_{\text{CFD}}/L_{wl}(Re)$. An acceptable solution is considered to be the total resistance value that lies within ±5% (or less if possible) of the measured value during experimental testing.

In CFD simulations, for all cases, velocity profiles were determined at 20%, 30%, 40%, 49%, 62% and 80% of L_{pp} along the centre line. At 100%L_{pp}, the boundary layer thickness is considered to be zero. The boundary layer thickness at each defined longitudinal position (%L_{pp}) was taken as the vertical distance from the ship's hull where the velocity reaches 99% of u_∞ with u_∞being the free-stream velocity. An illustrative representation of the determined velocity profiles is shown in Figure 2. The dots in Figure 2 denote the calculated boundary layer thickness at each cross-section. The resulting set of points can be approximated using a n^{th} degree polynomial via least squares regression, where the residual sum of squares (RSS) is minimized. Subsequently, the maximum value of the polynomial within the ship's length boundaries is identified and adopted as the boundary layer thickness for the entire ship.

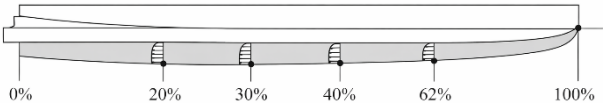

Figure 2. Boundary layer thickness evaluation

The boundary layer thickness determined by the CFD analysis is considered good if it is within the range of values obtained during the experiment or as close as possible. According to the notes from [49] it was often difficult to obtain satisfactory readings in the boundary layer and many of them are discounted, so this was the reason why only for one speed, the data about velocity profile is available. If the two conditions mentioned above (for total resistance and boundary layer thickness) are not met, the simulation setup parameters are adjusted until the results are considered valid, i.e., until both conditions are satisfied for all considered speeds and all scales (11 cases in total). The entire process is iterative and based on the principle of trial and error, adjusting the boundary layer thickness formula accor–ding to the results of the CFD analysis. Since the Lucy Ashton ship is relatively small by today's standards (58.1m), additional simulations were conducted with extrapolated ship dimensions using factors of 0.5, 0.18 and 0.12, for several speeds according to the matrix shown in the following table (Table 5). The "o" symbols indicate the originally conducted simulations corres–ponding to the cases defined through the workshop, while the "x" symbols indicate the additional simula–tions to extend the boundary layer formula to cover the range of the largest ship ever built (The Seawise Giant).

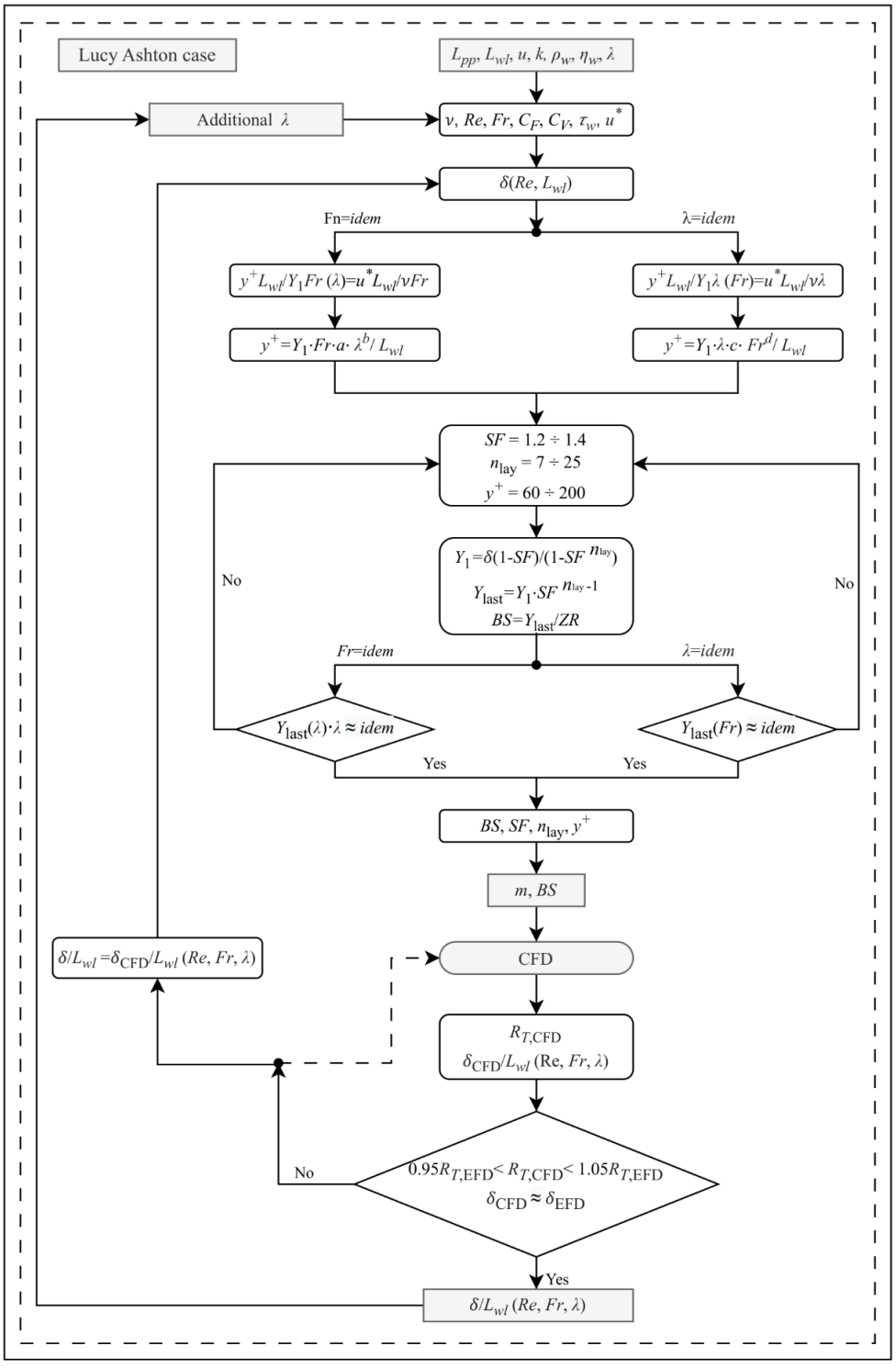

Figure 3. Methodology algorithm

The ratio $\delta_{CFD}/L_{wl}(Re)$ was found in the form of $e \cdot Re^h$, where e and h were determined in the same way as coefficients a, b, c and d (see (13-16)).

Table 5. Conducted simulation cases

λ	Fr=0.13	Fr=0.173	Fr=0.219	Fr=0.26	Fr=0.304
21.167	x		o		x
15.875			o		
11.906			o		
9.525			o		
7.938			o		
6.35	x		o		x
1	o	o	o	o	o
0.5	x		x		x
0.18	x		x		x
0.12	x		x		x

After conducting new simulations, the boundary layer thickness formula was further calibrated until the conditions for completing the calibration were met. The algorithm for determining the boundary layer thickness formula based on data for the Lucy Ashton ship is given in the Figure 3 (refer to end of paper).The dashed arrow in the same figure shows the possible calibration of other parameters during a single CFD calculation. Other parameters include domain size, turbulence model and its parameters, boundary conditions, solver, time step and others, which may affect the results. It is important to note that in the calculations for this study, these parameters were not changed compared to how they were defined for the Lucy Ashton workshop case and in previously published paper by authors [41].

Based on algorithm in Figure 3 (refer to the end of paper), a short code is developed in MATLAB software for evaluation of y^+, SF, n_{lay} and BS. As noted in Figure 3, range for y^+ is defined to be from 60 to 200. This is because, in a computational mesh, y^+ is evaluated at the centre of the first cell – corresponding to half of its thickness – rather than at the cell boundaries, which represent the full cell thickness.

The numerical models, boundary conditions, grid uncertainty analysis, and post-processing procedures were performed in accordance with the methodology described in the paper [41].

3. RESULTS

The results obtained according to the methodology defined in the previous chapter are presented below.

In Table 6 are shown values obtained with (7-10). In Table 7, initial values for defining near-wall region parameters are providedfor Fr=0.219 at different scales. Table 8 and Table 9(corresponding to Tables 6 and 7) also provide initial values for defining near-wall region parameters but for the full-scale ship at different Fr.

In Figure 4 the graphical representation of evaluated function $f(\lambda) = a \cdot \lambda^b$ is shown in accordance with data from Table 7.

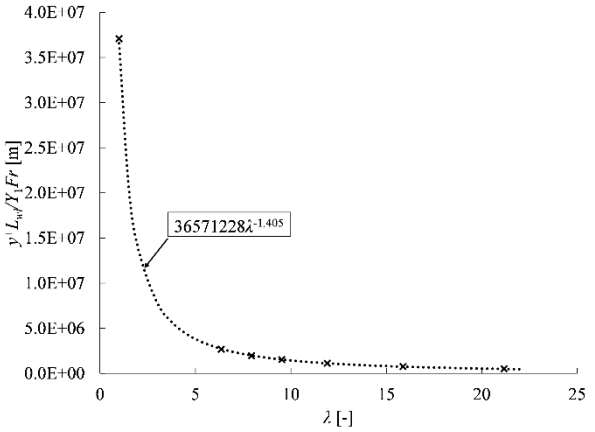

Figure 4. Graphical representation of evaluated (11) – (Lucy Ashton case Fr=0.219)

In Figure 5 graphical representation of evaluated function $g(Fr)=c \cdot Fr^d$ is shown in accordance with data from Table 7.

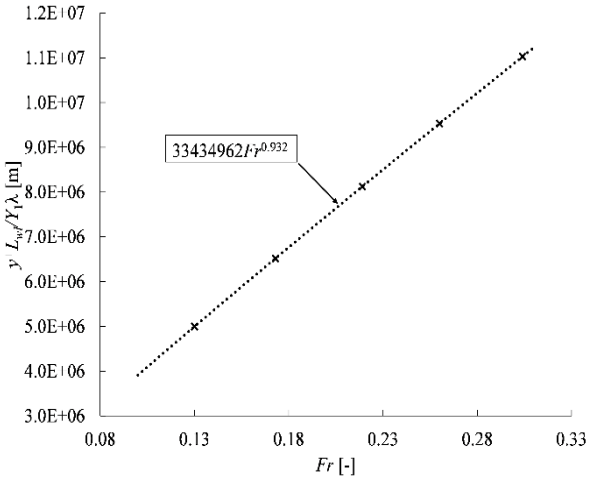

Figure 5. Graphical representation of evaluated (12)– (Lucy Ashton case λ =1)

Table 6. Initial values for near-wall region setup obtained with (7-10): (Lucy Ashton case, *Fr* = 0.219)

λ [-]	k [-]	V [m/s]	Re [-]	$C_{F,ITTC}$x10^3 [-]	C_vx10^3 [-]	τ_w [Pa]	u^* [m/s]
21.167	0.029	1.136	2511991	3.8739	3.9863	2.571	0.05073
15.875	0.035	1.312	3867554	3.5639	3.6886	3.172	0.05635
11.906	0.034	1.515	5954677	3.2896	3.4014	3.9	0.06249
9.525	0.042	1.694	8321652	3.0981	3.2282	4.627	0.06806
7.938	0.046	1.856	10938061	2.9538	3.0897	5.314	0.07294
6.35	0.051	2.075	15287850	2.7904	2.9328	6.305	0.07945
1	0.058	5.228	261594245	1.821	1.9266	27.018	0.16227

Table 7. Initial values for near-wall region setup obtained with MATLAB code: (Lucy Ashton case, *Fr* = 0.219)

λ [-]	δ [m]	y^+L_{wl}/Y_1Fr [-]	SF [-]	n_{lay}[-]	y^+[-]	Y_1[m]	Y_{last}[m]
21.167	0.02311	512086	1.20	7	35	0.00179	0.00534
15.875	0.02889	758417	1.24	7	44	0.00198	0.00718
11.906	0.03610	1121320	1.30	8	37	0.00151	0.00950

9.525	0.04292	1526621	1.29	9	38	0.0014	0.01073
7.938	0.04943	1963082	1.28	9	48	0.00168	0.01213
6.35	0.05876	2673162	1.28	10	48	0.00152	0.01404
1	0.24372	37073875	1.29	19	36	0.00056	0.05523

Table 8. Initial values for near-wall region setup obtained with (7-10): (Lucy Ashton case, λ =1)

Fr [-]	V [m/s]	Re [-]	$C_{F,\mathrm{ITTC}}$x10^3 [-]	C_vx10^3 [-]	τ_w [Pa]	u^* [m/s]
0.130	3.104	155284255	1.9567	2.0702	10.23	0.09985
0.173	4.130	206647508	1.8805	1.9896	17.411	0.13027
0.219	5.228	261594245	1.8210	1.9266	27.018	0.16227
0.260	6.207	310568510	1.7794	1.8826	37.212	0.19044
0.304	7.258	363126257	1.7428	1.8439	49.825	0.22037

Table 9. Initial values for near-wall region setup obtained with MATLAB code: (Lucy Ashton case, λ =1)

Fr [-]	δ [m]	$y^+L_{wl}/Y_1\lambda$ [-]	SF [-]	n_{lay}[-]	y^+[-]	Y_1[m]	Y_{last}[m]
0.130	0.26355	4995928	1.29	17	43	0.00102	0.06004
0.173	0.25249	6517776	1.29	18	41	0.00076	0.05735
0.219	0.24372	8119179	1.29	19	39	0.00056	0.05523
0.260	0.23752	9528551	1.29	19	44	0.00055	0.05382
0.304	0.23202	11025758	1.29	20	39	0.00042	0.05248

Based on (22), the h function could be evaluated for a range of Fr. The form of the function h is presented in Figure 6. The dots in Figure 6 present values of function h for a Fr=0.219. The bars indicate the ranges within which the function h varies depending on anotherFr. The approximated curve passes through the lowest sides of bars and is exponential in nature:

$$h(\lambda) \approx 43.79\exp(0.2794\cdot\lambda) + 29.85\exp(0.002018\cdot\lambda)$$

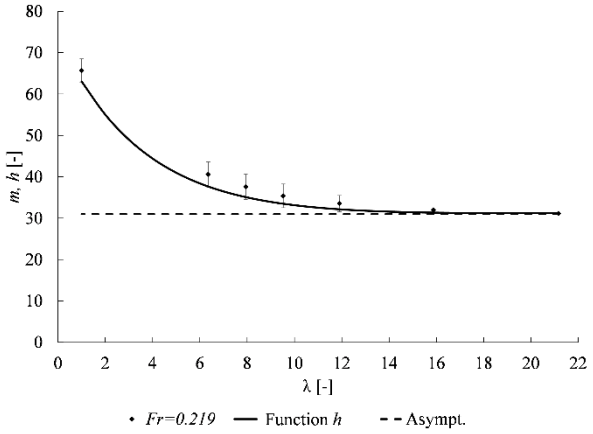

Figure 6. Evaluation of parameter function h and parameter m

The function h has a global minimum and it occurred at approximately $\lambda \approx 18.88$ with a minimum value of about 31.23. For the sake of simplicity in notation, the parameter value m=30 was adopted. Consequently, (23) takes its final form:

$$BS=(L_{pp}\cdot r)/(30\cdot\lambda). \quad (25)$$

The velocity profile obtained from CFD analysis can only be compared with one set of experimental measurement data, specifically at a speed of 10.18 kn ($Fr \approx$ 0.219) at 49% of the ship's length along the centreline. A comparative velocity profile, expressed in terms of boundary layer thickness (δ) and the ratio of disturbed to undisturbed flow velocity (u/u_∞), is shown in Figure7. In the figure, experimental data [49] are represented by "o" symbols, while a dashed line represents the approximated velocity profile based on experimental data analysis. The gray shaded area denotes the zone encompassing the velocity profile when accounting for all measured values. Data obtained from the CFD analysis are marked with "x" and the velocity profile is approximated with a solid line. A vertical dotted line indicates the 99%u_∞ level, which is defined as the boundary layer thickness at 49%L_{pp}.

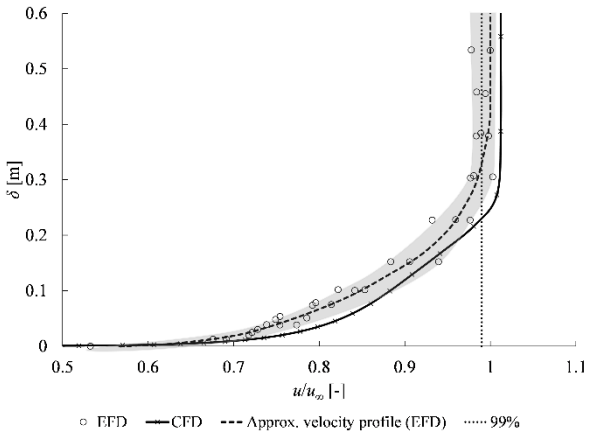

Figure 7. Velocity profile at CL at 49%L_{pp}, $Fr \approx$ 0.219

According to the methodology described, the boundary layer thickness determination procedure was applied to all transverse cross-sections at selected distances from the aft perpendicular (AP). These values were then approximated using an n-th degree polynomial along the ship's length. The process was repeated for each analyzed speed. By evaluating second-, third- and fourth-degree approximation polynomials, it was found that fourth-degree polynomials yield the smallest RSS. Results from the initial 11 CFD simulations related to boundary layer thickness are presented in Figure8 and Figure 9.

Figure 8 illustrates the boundary layer thickness distribution from 20% L_{pp} to 100% L_{pp} for different ship scales at Fr = 0.219. Here, the boundary layer thickness was multiplied by corresponding scaling factors to clearly display all six cases (scales) on a single diagram. Figure 9 shows the boundary layer thickness distribution along the ship's length for the full-scale ship at

various *Fr*. Dashed lines in Figure 8 and Figure 9 represent the fourth-degree approximation polynomials.

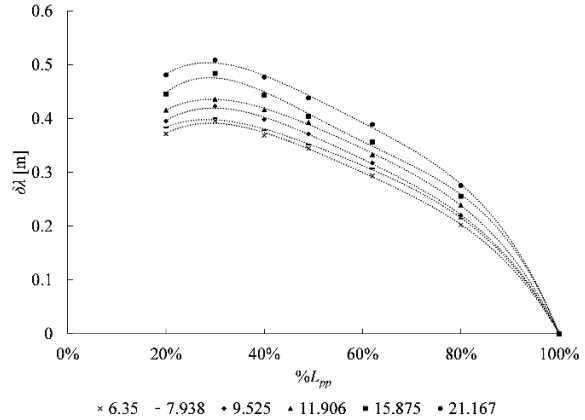

Figure 8. Boundary layer thicknesses for different *λ* (*Fr* = 0.219)

By solving the first derivative equation of the fourth-degree polynomial, it was determined that the maximum boundary layer thickness occurs at approximately 30%L_{pp} from the AP. The analysis further revealed that the effect of scale variation has a greater influence on boundary layer thickness than changes in speed.

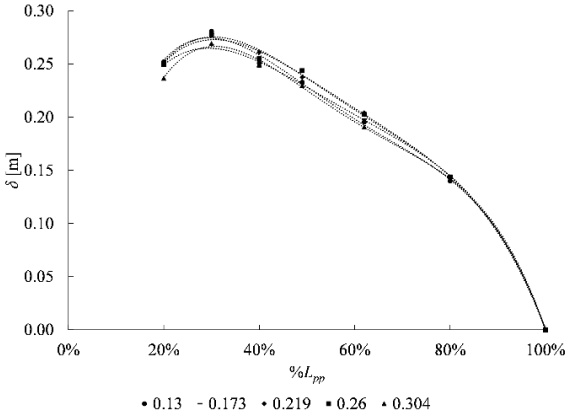

Figure 9. Boundary layer thicknesses for different *Fr* (*λ*=1)

The maximum of the fourth-degree polynomial, i.e., the maximum boundary layer thicknesses expressed in the dimensionless ratio (δ/L_{wl}) plotted as a function of *Re*, are shown in Figure10 for all cases examined in Table 5 (denoted with "x" for entire conducted simulations for Lucy Ashton case).

The final formula for boundary layer thickness evaluation is given below:

$$\frac{\delta}{L_{wl}} = \frac{0.075}{\mathrm{Re}^{0.15}}$$

In Figure10 are also given $\delta/L_{wl}(Re)$ lines obtained with (1-4) and (26).

The estimated total resistance coefficients obtained from CFD simulations using coarse, medium, and fine meshes are summarized in Table 10 and Table 12, to–gether with the corresponding EFD data and relative errors. The associated grid, data, and validation uncer–tainties for the Lucy Ashton case are reported in Table 11 and Table 13, covering various scales at a single speed and multiple speeds at full scale, respectively.

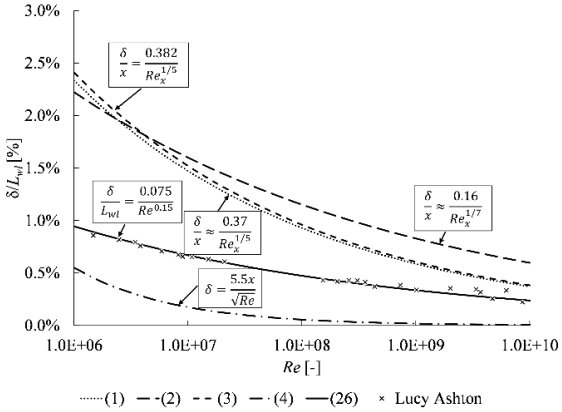

Figure 10. Non-dimensional boundary layer thickness change for different *Re (1-4, 26)*

Table 10. Results of Lucy Ashton case (various scales, one speed (same *Fr*))

			CFD			
	λ [-]	EFD	Coarse (S_3)	Medium (S_2)	Fine (S_1)	E %D
C_T x 10^3 [-]	21.167	4.3	4.495	4.444	4.404	-2.4
	15.875	4.038	-	-	4.125	-2.2
	11.906	3.838	-	-	3.808	0.8
	9.525	3.643	-	-	3.634	0.3
	7.938	3.621	-	-	3.482	3.8
	6.35	3.467	-	-	3.351	3.3
No. of cells x 10^6	-	-	0.63	1.311	2.637	-

Table 11. Validation for Lucy Ashton case (various scales, one speed (same *Fr*))

UG %S1	UD %D	UV %
7.04	1	7.1

Table 12. Results for Lucy Ashton case (various speeds, full scale)

			CFD			
	Fr [-]	EFD	Coarse (S_3)	Medium (S_2)	Fine (S_1)	E %D
C_T x 10^3 [-]	0.13	2.278	-	-	2.287	-2.4
	0.173	2.259	-	-	2.214	-2.2
	0.219	2.566	-	-	2.57	0.8
	0.26	3.024	-	-	3.101	0.3
	0.304	4.165	4.425	4.385	4.353	3.8
No. of cells x 10^6	-	-	0.846	1.633	3.481	-

Table 13. Validation for Lucy Ashton case (various speeds, full scale)

U_G %S_1	U_D %D	U_V %
6.4	1	6.5

In Table 14 and Table 15, the predicted y^+ values and the y^+ values obtained from CFD analysis are listed for cases of different scales at a constant *Fr*, as well as for the full-scale ship at varying *Fr*.

Table 14. y^+ values Lucy Ashton case (various scales, one speed)

λ [-]	target y^+[-]	obtained y^+[-]
21.167	35	38
15.875	44	43
11.906	37	36
9.525	38	37
7.938	48	47
6.35	48	47

Table 15. y^+ values Lucy Ashton case (various speeds, full scale)

Fr [-]	target y^+[-]	obtained y^+[-]
0.13	43	43
0.173	41	41
0.219	39	42
0.26	44	44
0.304	39	39

4. DISCUSSION

Although the parameter *m* for the full-scale case (λ=1) deviates by up to 100% from the adopted value (*m*=30) in (25), the obtained results are sufficiently reliable, as seen in Table 12 for the Lucy Ashton case. This also needs to be further tested with other types of full-scale ships because it has been observed that extrapolated ships (λ = 0.12 and λ = 0.18) exhibit oscillations in the residuals, as the cell aspect ratio is considerably large. This could be indicated in Figure 5, where the parameter for $\lambda < 1$ would be significantly greater than 30, while already at model scales the parameter *m* does not deviate substantially from 30. The next immediate step would be to verify the entire procedure and the derived formulas for other benchmark cases, including the Meteor case, for which full-scale measurements of total resistance exist and others benchmark cases such as JBC, KCS, DTC and others.

For cases where λ>10, the parameter *m* is shown not to change drastically. The development of the formula (26) is also heavily influenced by the parameter *ZR*, i.e., the definition of refinement zones around the ship.

The observed deviation of the parameter *m* for the full-scale case indicates that the parameter may depend not only on the *Re* but also on hull geometry and mesh refinement strategy. This suggests that the adopted value *m* = 30 should be interpreted as a practical engineering approximation rather than a universal constant. Nevertheless, the results demonstrate that the proposed mesh parameterization remains sufficiently robust even when deviations in *m* occur.

According to Figure7, the velocity profile obtained from CFD analysis partially lies outside the gray zone bounded by EFD data and exhibits an irregular shape. Additionally, the ratio of the water velocity in the disturbed flow zone to the constant velocity used as input in the simulation is greater than one, meaning the uniform flow velocity outside the boundary layer is higher than the undisturbed flow velocity and remains constant far from the ship's hull. The discrepancy in the velocity profile may stem from the neglect of hull roughness in the CFD simulations. While neglecting hull roughness is a plausible explanation, other factors such as turbulence modeling limitations (e.g., reliance on RANS vs. LES) may amplify discrepancies.

The number of cells in near-wall region is more influenced by scale than by changes in the *Fr*, as evidenced by the parameter n_{lay} in Table 7 and Table 9.This behavior is expected because the *Re* changes significantly with scale, directly affecting viscous effects and boundary layer development. In contrast, variations in the *Fr*primarily influence the wave system rather than the viscous flow close to the hull. Based on Figure 8, there is no geometric similarity in boundary layer thickness across different scales, even though dynamic similarity (*Fr*=*idem*) is satisfied. However, the trend in boundary layer thickness distribution remains similar. The non-dimensional boundary layer thickness decreases with increasing *Re* as a classical theory based on earlier experiments with pipes and flat plates. For all cases, a 4th-degree polynomial (Figure8 and Figure9) provides a good approximation of the boundary layer thickness distribution along the centerline. The position of maximum boundary layer thickness depends on the geometry of the flat bottom and the location of the stern shoulders and in this case is about 30% of L_{pp} towards the bow. Notably, the boundary layer does not exhibit a uniformly increasing trend along the centerline. Below 20% of L_{pp}, a sharp increase in boundary layer thickness occurs. The non-uniform growth of the boundary layer along the hull can be explained by the pressure gradients generated by the hull geometry. In the forward part of the hull, the flow is subjected to favorable pres–sure gradients which delay boundary layer thickening, while the stern region is characterized by adverse pres–sure gradients and wake formation that accelerate boundary layer growth.

The estimation of form factors is well executed, resulting in accurate predictions of y^+ values, as seen in Table 14 and Table 15.

Regarding the total resistance coefficient obtained from CFD analysis, deviations for individual cases (speeds) are below 4%, (Table 10 and Table 12). Grid uncertainty analysis, involving three different grids, validated CFD results, as $E\%D < U_V$. The grid uncertainty analysis was performed for only one speed (see Table 10, Table 11, Table 12, Table 13).

The choice of formula for estimating prismlayer total thickness does not play a critical role in obtaining valid results. Equation(1) was employed in the first ite–ration as an initial approximation for the estimation of characteristic parameters, providing a necessary starting point for the iterative procedure. In subsequent itera–tions, alternative formulations were applied; however, only the results corresponding to the initial and final iterations are presented herein, as inclusion of interme–diate steps would unnecessarily extend the discussion without providing additional insight. Following the methodology described, a number of layers within the estimated prism layer total thickness (near-wall region) are shown in Table 16 and Table 17.

Table 16. Number of layers (Lucy Ashton - various scales, *Fr*=0.219)

	Eq. (26)	Eq. (1)
λ [-]	n_{lay} [-]	n_{lay} [-]
21.167	7	8
15.875	7	9
11.906	8	11
9.525	9	12
7.938	9	12
6.35	10	13

The number of layers defined according to (1) results up to 30% more layers, thereby increasing the total cell count in the mesh and directly extending the simulation runtime. What gives (26) an advantage is

that the total thickness is almost twice as small compared to (1), which allows for a bigger number of layers in the region with a high velocity gradient.

Table 17. Number of layers (Lucy Ashton – full scale, various *Fr*)

	Eq. (26)	Eq. (1)
Fr [-]	n_{lay} [-]	n_{lay} [-]
0.130	17	20
0.173	18	20
0.219	19	20
0.260	19	21
0.304	20	21

In Figure 11, the cell distribution and velocity profile in the near-wall region are shown, with the boundary layer thickness estimated using (1) (top) and (26) (bottom) at 49% of L_{pp} of the Lucy Ashton in full scale for $Fr = 0.219$.

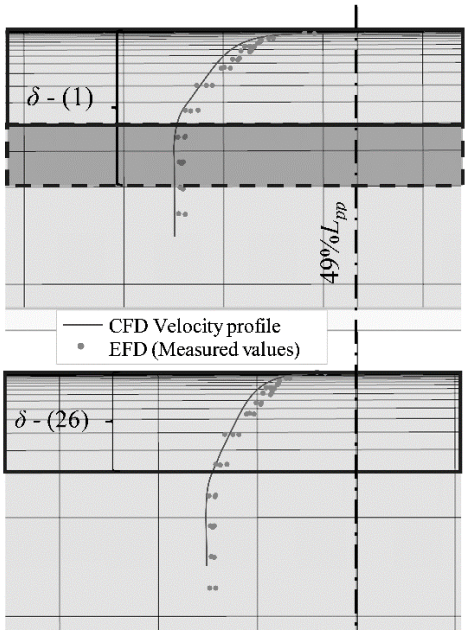

Figure 11. Comparison of cell distribution and velocity profiles (evaluated through CFD and EFD) in the near-wall region obtained with (1) and (26) at 49%L_{pp} of Lucy Ashton in full scale for *Fr* = 0.219.

The velocity profiles obtained from CFD analysis are shown with a solid line, while the measured velocities from EFD are indicated with dots. The estimated boundary layer thickness based on CFD results is marked with a solid line rectangle, while the absolute difference between the prism layer total thickness estimated by (1) and boundary layer thickness determined through CFD is marked with a grey zone in dashed rectangle (in the upper part of the figure). In the lower there is no dashed rectangle because prism layer total thickness and boundary layer are the same.

According to Table 17, the estimated number of layers in the near-wall region based on (1), n_{lay}, is 20. However, based on CFD results, 18 layers are sufficient to cover the entire boundary layer. According to (26), the number of layers in the near-wall region is $n_{lay} = 19$, and there are no additional layers that would increase the total number of cells and thus prolong the simulation time.

In any case, this difference in the number of cells is negligible and has practically no effect on the resistance prediction in CFD simulations in full scale.

In Figure 12, the cell distribution and velocity profile in the near-wall region are shown, with the prism layer total thickness estimated using (1) (top) and (26) (bottom) at 49% of L_{pp} of the Lucy Ashton in model scale ($\lambda = 21.167$) for $Fr = 0.219$.

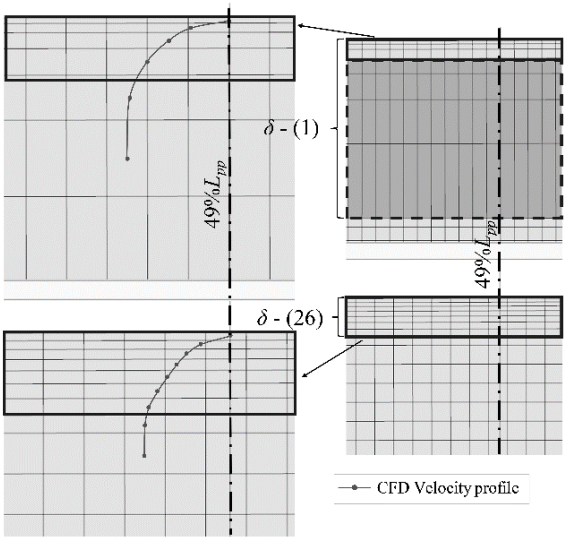

Figure 12. Comparison of cell distribution and velocity profiles (evaluated through CFD and EFD) in the near-wall region obtained with (1) and (26) at 49%L_{pp} of Lucy Ashton in model scale (λ=21.167) for Fr=0.219

The velocity profiles obtained from the CFD analysis are shown with a solid line. The estimated boundary layer thickness based on CFD results is mar–ked with a solid line rectangle, while the absolute difference between the prism layer total thickness estimated by (1) and that determined through CFD is marked with a grey zone in dashed rectangle (Figure 12, top right).

According to Table 16, the estimated number of layers in the near-wall region based on (1), n_{lay}, is 8. However, according to the CFD results, 4 to 5 layers are sufficient to cover the entire boundary layer. In the additional three layers, one cell dimension compared to the other is large (grey zone in dashed rectangle in Figure 12, top right), i.e., the height of the last cell (Y_{last}) is exceptionally large (the aspect ratio is large), which can lead to numerical instability.

To avoid numerical instability, the cell size in the other dimension (lengthwise) should match the height of the last cell. However, this would mean that the ship hull would be represented with a very coarse mesh in model scale, leading to larger deviations in resistance prediction from CFD compared to EFD.

On the other hand, to maintain the same cell dimen–sion along the length, it is possible to increase the num–ber of layers n_{lay} in the near-wall region, but this would significantly prolong the simulation time due to the unnecessary increase in the total number of cells.

According to (26), the number of layers in the near-wall region is $n_{lay} = 7$, which represents the balance between result reliability, boundary layer thickness estimation, and simulation runtime.

Table 18 provides the standard deviation of the differences between CFD and EFD results for Lucy Ashton using two distinct formulas ((26) and (1)). In both examined cases, the use of (26) yielded results with slightly smaller standard deviations and shorter simulation times.

Table 18. Standard deviation between CFD and EFD with implementation of (26) and (1).

	Lucy Ashton	
	Various λ	Various Fr
Eq. (26)	2.2	2.1
Eq. (1)	2.6	2.3

From a practical perspective, the advantage of (26) lies in the more balanced distribution of cells within the near-wall region. By reducing unnecessary prism layer thickness, the method allows a greater portion of the mesh resolution to be concentrated in regions with strong velocity gradients. This leads to improved numerical stability while maintaining comparable accuracy in resistance prediction.

The additional analysis includes verification of the use of (4); however, according to the described methodology and the defined limits for SF, n_{lay} and y^+, it was not possible to determine these three parameters. For this reason, the CFD analysis was not conducted for this case.

The main contribution of the present study lies in the systematic parameterization of CFD mesh parameters based on boundary layer characteristics. Unlike previous investigations of the Lucy Ashton case [39, 40, 41], this work focuses on establishing relationships between the Re, boundary layer thickness and key mesh parameters used in CFD simulations.

5. CONCLUSION

This study investigated the relationship between boundary layer characteristics and mesh parameterization in CFD simulations of ship resistance using the Lucy Ashton benchmark case. The analysis included six model scales and full-scale conditions for which experimental resistance data and boundary layer measurements are available. The objective was to examine the influence of scaling, Fr and Re on boundary layer development and to evaluate their implications for mesh definition in the near-wall region.

A methodology was proposed for estimating key mesh parameters in the near-wall region, including the prism layer total thickness, number of layers and first cell height. Initial mesh parameters were defined for different scales and Fr, allowing a systematic setup of CFD simulations. The comparison of velocity profiles demonstrated a reasonable agreement between CFD and experimental data, with the predicted boundary layer thickness falling within the expected experimental range.

The results showed that scale effects have a stronger influence on boundary layer development than variations in Fr, while the nondimensional boundary layer thickness decreases with increasing Re, consistent with classical theoretical expectations. CFD predictions of the total resistance coefficient showed deviations below 3.8% compared with experimental data, confirming the reliability of the numerical setup.

The comparison of different formulations for estimating prism layer total thickness indicated that (26) provides a more balanced compromise between numerical accuracy and computational efficiency for the investigated case. The proposed procedure therefore provides practical guidance for defining near-wall mesh parameters in CFD simulations of ship flows.

It should be noted that the methodology was developed based on a single hull form and simulations performed using STAR-CCM+. Although the results demonstrate promising agreement with experimental data, further validation on additional benchmark hull forms is required in order to confirm the broader applicability of the proposed approach.

Future work should focus on extending the validation to other benchmark cases, including ships with different geometrical characteristics, as well as exploring advanced mesh adaptation strategies and optimization techniques to further improve computational efficiency.

ACKNOWLEDGMENT

The research is supported by Ministry of Science, Technology Development and Innovation of Republic of Serbia, Contract No. 451-03-34/2026-03/200105. Authors would like to acknowledge Ocean Pro Marine Engineers LTD for its help in guidance and support for CFD assessment.

REFERENCES

[1] Simić, A. and Radojčić, D.: On energy efficiency of inland waterway self-propelled cargo vessels, FME Transactions, Vol. 41, No. 2, 2013.

[2] Vasilev, M. and Kalajdžić, M.: Influence of lightweight change on ship performance, FME Transactions, Vol. 50, No. 4, 2022. doi:10.5937/fme2204615V

[3] Elhadad, A.M., El-Ela, A.M.A. and Hussien, M.M.: MATLAB implementation using Holtrop and Mennen method of bare hull resistance prediction for a surface combatant ship coupled with CFD, CFD Letters, Vol. 15, No. 10, pp. 1–11, 2023. doi:10.37934/cfdl.15.10.111

[4] Widiawaty, C.D., Siswantara, A.I., Budiyanto, M.A., Andira, M.A., Adanta, D., Hilman, M., Syafei, G., Farhan, T.A. and Rizianiza, I.: Analysis of mesh resolution effect on numerical results of CFD-ROM turbulent flow in stationary parallel plates, CFD Letters, Vol. 16, No. 8, pp. 1–17, 2024. doi:10.37934/cfdl.16.8.117

[5] Davidson, J., Nava, V., Andersen, J. and Kramer, M.: Exploiting axisymmetry to optimize CFD simulations—heave motion and wave radiation of a spherical buoy, Symmetry, Vol. 16, No. 9, 1252, 2024. doi:10.3390/sym16091252

[6] Zeraatgar, H., Ghaemi, M. and Sadeghi, M.: Analysis of instantaneous ship resistance increase in waves using CFD-URANS, Polish Maritime Research, Vol. 32, No. 1, 2025. doi:10.2478/pomr-2025-0001

[7] Liu, J., Hu, L., Zhang, B., Zhang, K., Bi, J., Zheng, Q.: Enhancing ship hydrodynamic performance via machine-learning-driven CFD parametric optimi–zation, Engineering Applications of Computational Fluid Mechanics, Vol. 19, No. 1, 2025. doi:10.1080/19942060.2025.2565801

[8] Mandru, A., Rusu, L., Bekhit, A., Pacuraru, F.: Numerical study of a model- and full-scale conta–iner ship sailing in regular head waves, Inventions, Vol. 9, No. 1, 22, 2024. doi:10.3390/inventions 9010022

[9] Mikulec, M., Piehl, H.: Verification and validation of CFD simulations with full-scale ship speed/ power trial data, Brodogradnja, Vol. 74, No. 1, 2022. doi:10.21278/brod74103

[10] Yang, C., Zeng, K., Chu, J., Han, Y., Gu, M.: Study of influencing factors on CFD methods and separated flow by the virtual static captive test, *IOP Conference Series: Materials Science and Engine–ering*, Vol. 1288, 012049, 2023. doi:10.1088/1757-899X/1288/1/012049

[11] Espaa, R.E., Alvarez, L.V. and Samarasinghe, J.T.: Grid-independence studies applied to a field-scale CFD model using the DES technique along the Colorado River, Earth Surface Processes and Landforms, 2025. doi:10.1002/esp.70030

[12] Wu, P.-C.: A CFD-based correction for ship mass and longitudinal center of gravity to improve resistance simulation, Mathematics, Vol. 13, No. 11, 1788, 2025. doi:10.3390/math13111788

[13] Jin, S., Peng, H., Qiu, W., Oldfield, C., Stockdill, B.: Best modeling practice for self-propulsion simulation of a ship model in calm water, Physics of Fluids, Vol. 35, 2023. doi:10.1063/5.0167387

[14] Sun, W. et al.: Numerical analysis of full-scale ship self-propulsion performance with direct comparison to sea trial results, Journal of Marine Science and Engineering, Vol. 8, No. 1, 24, 2020. doi:10.3390/ jmse8010024

[15] Wang, X., Ma, Y., Feng, D., Yao, C., Cai, Z.: Numerical study of the hydrodynamic performance of a two-propeller configuration, Journal of Marine Science and Engineering, Vol. 13, No. 5, 992, 2025. doi:10.3390/jmse13050992

[16] Saydam, A.Z., Koksu, G.N., Insel, M., Gokay, S.: Uncertainty quantification of self-propulsion ana–lyses with RANS-CFD and comparison with full-scale ship trials, Brodogradnja, Vol. 73, No. 4, 2022. doi:10.21278/brod73406

[17] Moon, M.H., Zaman, S.A., Hussain, M.D., Uddin, M.M.: Preliminary assessment of power savings by Flettner rotors installed on a cargo ship, MIST International Journal of Science and Technology, Vol. 13, No. 1, pp. 73–82, 2025. doi: 10.47981/ j.mijst.13(01)2025.508

[18] Schlichting, H. and Gersten, K.: *Boundary-Layer Theory*, 9th ed., Springer, Berlin, 2017.

[19] Prandtl, L.: On fluid motion with very small fric–tion, *Proc. 3rd Int. Math. Congress*, Heidelberg, 1904 (English translation).

[20] Prandtl, L.: Ergebnisse der Aerodynamischen Ver–suchsanstalt Göttingen, Vol. 3, 1927.

[21] Nikuradse, J.: Investigations on velocity distri–bution in turbulent flows, Forschungsheft, No. 281, 1926.

[22] Nikuradse, J.: Laws of flow in rough pipes, *VDI*-Forschungsheft, No. 361, 1933.

[23] White, F.M. and Majdalani, J.: *Viscous Fluid Flow*, 4th ed., McGraw-Hill, New York, 2021.

[24] Kothandaraman, C.P. and Rudramoorthy, R.: *Fluid Mechanics and Machinery*, 2nd ed., New Age International, New Delhi, 2007.

[25] Pena, B., Muk-Pavic, E., Fitzsimons, P.: Detailed analysis of the flow within the boundary layer and wake of a full-scale ship, Ocean Engineering, Vol. 218, 108022, 2020. doi: 10.1016/j.oceaneng.2020. 108022

[26] Garthune, R.S., Rosenberg, B., Cafiero, D., Olson, C.R.: The performance of model ships in restricted channels in relation to ship canal design, Defense Documentation Center for Scientific and Technical Information, Alexandria, VA, 1948.

[27] Klemm, V.P., Buckingham, W.L.: Investigation of the scale effect of appendage resistance of DD-710 class ship models, M.Sc. Thesis, Webb Institute of Naval Architecture, Glen Cove, NY, 1954.

[28] Larsson, L.: Calculation method for three-dimen–sional turbulent boundary layers on ship-like bodies, *Proc. 1st Int. Conf. on Numerical Ship Hydrodynamics*, Washington, D.C., 1975.

[29] Larsson, L.: *SSPA-ITTC Workshop on Ship Boun–dary Layers—Proceedings*, Liber Distribution, Väl–lingby, Sweden, 1980.

[30] Cebeci, T., Chang, K.C., Kaups, K.: General method for calculating three-dimensional laminar and turbulent boundary layers on ship hulls, Ocean Engineering, Vol. 7, No. 2, pp. 229–280, 1980. doi:10.1016/0029-8018(80)90058-X

[31] Patel, V.C. and Sarda, O.P.: Mean-flow and turbulence measurements in the boundary layer and wake of a ship double model, Experiments in Fluids, Vol. 8, No. 6, pp. 319–335, 1990. doi:10.1007/BF00217197

[32] Toda, Y., Stern, F., Tanaka, I., Patel, V.C.: Mean-flow measurements in the boundary layer and wake of a Series-60 (CB=0.6) model ship with and without propeller, Journal of Ship Research, Vol. 34, No. 4, pp. 225–252, 1990. doi:10.5957/jsr. 1990.34.4.225

[33] Chawner, J.R., Dannenhoffer, J., Taylor, N.J.: Geo–metry, mesh generation and the CFD-2030 vision, *Proc. 46th AIAA Fluid Dynamics Conference*, Washington, D.C., 2016. doi:10.2514/6.2016-3485

[34] Sadakata, K., Hino, T., Takagi, Y.: Estimation of full-scale performance of energy-saving devices using a boundary-layer similarity model, Journal of Marine Science and Technology, Vol. 29, 2024. doi:10.1007/s00773-023-00981-2

[35] Nguyen, H.V., Nguyen, V.H.: Viscous resistance acting on a symmetrical hull with different turbu–lent models, *Proc. NICS*, 2022. doi:10.1109/NICS 56915.2022.10013465

[36] Tezdogan, T., Kim, D., Incecik, A.: Hydrodynamic analysis of ship manoeuvrability at ports using CFD, International Maritime Transport and Logis–tics Journal, Vol. 12, No. 1, pp. 213–225, 2023. doi:10.21622/marlog.2023.12.1.213

[37] Deng, R., Huang, D., Li, J., Cheng, X., Lei, Y.: Discussion of grid generation for catamaran resis–tance calculation, Journal of Marine Science and Application, Vol. 9, No. 2, pp. 187–191, 2010. doi:10.1007/s11804-010-9080-2

[38] Deng, R., Huang, D., Zhou, G.L., Sun, H., Chang, L., Ma, C.: Research on mesh generation affecting resistance calculation, Applied Mechanics and Materials, Vols. 138–139, pp. 886–893, 2011. doi:10.4028/www.scientific.net/AMM.138-139.886

[39] Lopes, R., Eslamdoost, A., Bensow, R.E., Ponk–ratov, D. *et al.*: Summary of the Lucy Ashton resis–tance prediction workshop, Ocean Engineering, Vol. 343, 122951, 2026. doi: 10.1016/j.oceaneng .2025.122951

[40] Lopes, R., Eslamdoost, A., Johansson, R., Roy Choudhury, S., Bensow, R.E., Hogstrom, P. and Ponkratov, D.: Resistance prediction using CFD at model and full scale and comparison with measu–rements, Ocean Engineering, Vol. 321, 120367, 2025. doi: 10.1016/j.oceaneng.2025.120367

[41] Vasilev, M., Kalajdžić, M., Ponkratov, D.: CFD approach to full-scale resistance – The Lucy Ashton case, Brodogradnja, Vol. 77, No. 3, 77307, 2025. doi:10.21278/brod77307

[42] ITTC: 1978 ITTC performance prediction method, *ITTC Quality System Manual*, Recommended Procedures and Guidelines, 2021.

[43] ITTC: Final report of the specialist committee on powering performance prediction, *Proc. 25th ITTC*, Fukuoka, Japan, 2008.

[44] Molland, A.F., Turnock, S.R., Hudson, D.A.: *Ship Resistance and Propulsion*, Cambridge University Press, Cambridge, 2011.

[45] Vasilev, M., Kalajdžić, M., Ivković, I.: CFD-powe–red ship trim optimization integrating ANN for user-friendly software development, Journal of Marine Science and Engineering, Vol. 12, 1265, 2024. doi:10.3390/jmse12081265

[46] Korkmaz, K.B., Werner, S., Sakamoto, N. *et al.*: CFD-based form factor determination method, Ocean Engineering, Vol. 220, 108451, 2021. doi: 10.1016/j.oceaneng.2020.108451

[47] ITTC: Practical guidelines for ship CFD appli–cations, *ITTC Quality System Manual*, 2024.

[48] ITTC: Uncertainty analysis in CFD verification and validation, *ITTC Quality System Manual*, 2024.

[49] Smith, L.: Resistance experiments on the Lucy Ashton—Part IV, Quarterly Transactions of the Institution of Naval Architects, Vol. 97, No. 4, pp. 525–561, 1955.

NOMENCLATURE

Sym	Unit	Name
∇	m^3	Displacement volume
a	-	Coefficient of function $f(\lambda)$
B	m	Breadth
b	-	Exponent of function $f(\lambda)$
BS	m	Cell base size
c	-	Coefficient of function $g(Fr)$
C_b	-	Block coefficient
C_F	-	Friction resistance coefficient
$C_{F,\mathrm{ITTC}}$	-	Friction resistance coefficient based on ITTC guidelines
C_m	-	Midship coefficient
C_p	-	Prismatic coefficient
C_T	-	Total resistance coefficient
C_V	-	Viscous resistance coefficient
D	-	EFD data
d	-	Exponent of function $g(Fr)$
e	-	Coefficient
E	-	Comparison error
f	-	Wall-resolution control function based on λ
Fr	-	Froude number
g	-	Wall-resolution control function based on Fr
H	m	Depth
h	-	Mesh scaling function
i	-	Exponent
j	-	Counter
k	-	Form factor
l	-	Number of cases
L_{pp}	m	Length between perpendiculars
L_{wl}	m	Waterline length
n_{lay}	-	Number of layers in boundary layer
r	-	Refinement factor
Re	-	Reynolds number
$R_{T,\mathrm{CFD}}$	N	Total resistance based on CFD analysis
$R_{T,\mathrm{EFD}}$	N	Total resistance based on EFD analysis
S	-	CFD solution
s	-	Exponent of parameter m
SF	-	Stretch factor
T	m	Draft
u	m/s	Fluid speed
u^*	m/s	Friction velocity
u_∞	m/s	Undisturbed stream velocity
U_D	-	Data uncertainty
U_G	-	Grid uncertainty
U_V	-	Validation uncertainty
WS	m^2	Wetted surface without rudder
WS_{total}	m^2	Wetted surface with rudder
x	m	Length / Cell length in x direction
y	-	Cell length in y direction
y^+	-	Non-dimensional wall distance
Y_1	m	First cell thickness in the boundary layer
Y_{last}	m	Last cell thickness in the boundary layer

z	-	Cell length in z direction
ZR	-	Zone refinement factor
δ	m	Boundary layer thickness
δ_{CFD}	m	Boundary layer thickness based on CFD analysis
δ_{pltt}	m	Prism layer total thickness, near-wall region thickness
$\Delta_{(\mathrm{sw})}$	t	Displacement in sea water
ΔC_F	-	Roughness allowance
η_a	kg/ms	Dynamic viscosity of air
η_w	kg/ms	Dynamic viscosity of water
λ	-	Scale
ρ_a	kg/m^3	Air density
ρ_w	kg/m^3	Water density
τ_w	N/m^2	Shear stress
υ	m^2/s	Kinematic viscosity of water

ПАРАМЕТАРСКО ДЕФИНИСАЊЕ МРЕЖЕ: СТУДИЈА СЛУЧАЈА – ЛУСИ ЕШТОН

М. Василев, М. Калајџић

ОвастудијаобухватабродЛуси Ештон (енг. *Lucy Ashton*), јединствен референтни случај који пружа податке о мереном тоталном отпору брода у стварној величини и мерења дебљине граничног слоја. Спроведена је серија CFD симулација за више различитих размера и Фрудових бројева, са циљем репродукције експерименталних података о отпору брода и граничном слоју. Резултати су показали одлично слагање са мерењима, при чему су прогнозе отпора бродабиле у оквиру ±5%, а профили гра–ничног слоја дуж трупа реалистични. На основу ових налаза изведене су практичне формуле за дебљину граничног слоја и величину основне ћелије мреже. Иако су ове формуле изведене узимајући у обзир само брод Луси Ештон, они представљају обећава–јућу основу за примену и на другим бродовима, поготов у раземри модела. Препоручују се даља истраживања ради потврде њихове поузданости за различите форме трупау стварној величини.